Supplementary Materials for

Single-Crystal Elasticity of (Al,Fe)-bearing Bridgmanite up to 82 GPa

Suyu Fu[a,1,*], Yanyao Zhang[a], Takuo Okuchi[b,2], Jung-Fu Lin[a,*]

[a]Department of Geological Sciences, Jackson School of Geosciences, The University of Texas at Austin, Austin, TX, USA

[b]Institute for Planetary Materials, Okayama University, Misasa, Japan

[1]Now at School of Earth and Space Exploration, Arizona State University, Tempe, Arizona, USA.

[2]Now at Institute for Integrated Radiation and Nuclear Science, Kyoto University, Kyoto, Japan.

[*]Corresponding author: Jung-Fu Lin (afu@jsg.utexas.edu), Suyu Fu (fsyxhy@gmail.com)

Supplementary materials for single-crystal elasticity of (Al,Fe)-bearing bridgmanite consists of:

Texts S1-S3

Figures S1-S4

Tables S1-S3

Text S1. Data analyses on equation of state of single-crystal Fe10-Al14-Bgm. Collected high-pressure XRD patterns of single-crystal Fe10-Al14-Bgm were analyzed to determine its unit cell parameters and volumes (Figure S1 and Table S2). We fit the pressure-volume relationship at 300 K using a third-order Birch-Murnaghan equation of state (EoS) (Birch, 1978):

$$P = \frac{3}{2}K_{\mathrm{T0}}\left[(V_0/V)^{\frac{7}{3}} - (V_0/V)^{\frac{5}{3}}\right]\left\{1 + \frac{3}{4}(K'_{\mathrm{T0}} - 4)\left[(V_0/V)^{\frac{2}{3}} - 1\right]\right\} \quad (1)$$

where K_{T0} (V_0) is the isothermal bulk modulus (unit cell volume) at ambient conditions, and K'_{T0} is the pressure derivative of K_{T0}. The best fits show $K_{\mathrm{T0}} = 256\ (\pm 2)\ GPa$, $K'_{\mathrm{T0}} = 4$ (fixed), or $K_{\mathrm{T0}} = 259\ (\pm 4)\ GPa$, $K'_{\mathrm{T0}} = 3.8(\pm 0.2)$, with a fixed V_0 as 163.75 Å^3, consistent with early studies on (Al,Fe)-bearing bridgmanite within uncertainties (Boffa Ballaran et al., 2012; Mao et al., 2017).

Text S2. Fe partitioning between ferropericlase and bridgmanite as well as the spin crossover in ferropericlase. Early studies show that Fe partitioning coefficient between bridgmanite and ferropericlase (K_{D}, given by $[Fe^{2+}+Fe^{3+}]_{\mathrm{Bgm}}/[Mg^{2+}]_{\mathrm{Bgm}})/(Fe^{2+}]_{\mathrm{Fp}}/[Mg^{2+}]_{\mathrm{Fp}}$) could vary significantly with depth as a result of the spin crossover in ferropericlase (Irifune et al., 2010). Using literature K_{D} in a pyrolitic system (Irifune et al., 2010) for our modeling, Fe content in ferropericlase would change with depth in the lower mantle. Here we assume a linear Fe effect on K_{S}, μ and ρ of high-spin (HS) and low-spin (LS) ferropericlase and fit the literature data together (Figure S2) (Fei et al., 2007; Mao et al., 2011; Marquardt et al., 2009; Speziale et al., 2001; Yang et al., 2016; Yang et al., 2015). The best fits to density using Birch-Murnaghan EoS with fixed $K'_{T0} = 4$ show:

$$\rho_{0\_\mathrm{HS}}(Fe) = 3.58 + 2.40Fe_{\mathrm{Fp}};\ K_{T0\_\mathrm{HS}}(Fe) = 159.5 - 11.8Fe_{\mathrm{Fp}} \quad (2)$$

$$\rho_{0\_\mathrm{LS}}(Fe) = 3.58 + 2.83Fe_{\mathrm{Fp}};\ K_{T0\_LS}(Fe) = 153.3 + 40.5Fe_{\mathrm{Fp}} \quad (3)$$

where Fe_{Fp} is the Fe content in ferropericlase, given as Fe_{Fp}=Fe/(Fe+Mg), and subscripts "HS" and "LS" indicate properties of HS and LS ferropericlase, respectively, with the same denotation for other

parameters in the followings. Analyses of literature reports (Wu et al., 2013; Yang et al., 2015) were used for Fe effect on μ of ferropericlase:

$$\mu_{0\_HS}(Fe) = 129 - 81.8Fe_{\mathrm{Fp}};\ \mu'_{0\_HS}(Fe) = 2.32 - 1.97Fe_{\mathrm{Fp}} \quad (4)$$

$$\mu_{0\_LS}(Fe) = 142 - 81.8Fe_{\mathrm{Fp}};\ \mu'_{0\_LS}(Fe) = 2.23 - 1.97Fe_{\mathrm{Fp}} \quad (5)$$

To evaluate the spin crossover effect on K_S, μ, and ρ of ferropericlase, we followed the literature modeling procedure (Mao et al., 2011; Wu et al., 2013; Yang et al., 2015) using:

$$V(n) = nV_{\mathrm{LS}} + (1-n)V_{\mathrm{HS}} \quad (6)$$

$$\frac{V(n)}{Ks(n)} = n\frac{V_{\mathrm{LS}}}{Ks_{\mathrm{LS}}} + (1-n)\frac{V_{\mathrm{HS}}}{Ks_{\mathrm{HS}}} - (V_{\mathrm{LS}} - V_{\mathrm{HS}})\frac{\partial n}{\partial P}|_T \quad (7)$$

$$\frac{V(n)}{\mu(n)} \approx n\frac{V_{\mathrm{LS}}}{\mu_{\mathrm{LS}}} + (1-n)\frac{V_{\mathrm{HS}}}{\mu_{\mathrm{HS}}} \quad (8)$$

where n is the LS fraction at high P-T. We note that studies indicate that the Fe effect on the onset pressure and width of the spin crossover is negligible for relatively Fe-poor ferropericlase (<25 mol% Fe), but becomes complex for the Fe-rich (Mg,Fe)O counterpart (Speziale et al., 2007). Our modeling is limited to ferropericlase containing less than 25 mol% Fe, which is most relevant to the lower-mantle composition.

Text S3. Thermoelastic modeling of ferropericlase and davemaoite at high P-T. High P-T elastic data on different compositional ferropericlase (e.g., Fan et al., 2019; Mao et al., 2011; Yang et al., 2016) are used to evaluate the effects of Fe as well as the spin crossover on its elastic properties (Figure S2 and Table S3) (Fan et al., 2019; Marquardt et al., 2009; Yang et al., 2015). Our modeled high P-T velocity profiles are compared with *ab initio* calculations on $Mg_{0.8126}Fe_{0.1875}O$ ferropericlase (Wu et al., 2013) to evaluate the reliability of the constrained θ_0, γ_0, and q_0 values and their corresponding uncertainties (Stixrude and Lithgow-Bertelloni, 2005; Wentzcovitch et al., 2004; Wolf et al., 2015). We also

determined the thermoelastic parameters of $CaSiO_3$ davemaoite by refitting and benchmarking high P-T elastic data from experiments (Gréaux et al., 2019; Sun et al., 2016) and theoretical calculations (Kawai and Tsuchiya, 2015; Li et al., 2006) (Figure S3 and Table S3). Our modeled results fall into the range of theoretical calculations (Kawai and Tsuchiya, 2015; Li et al., 2006). We note that the data of davemaoite by Thomson et al. (2019) were not used here because they reported a much lower density profile than those by Gréaux et al. (2019) and Sun et al. (2016).

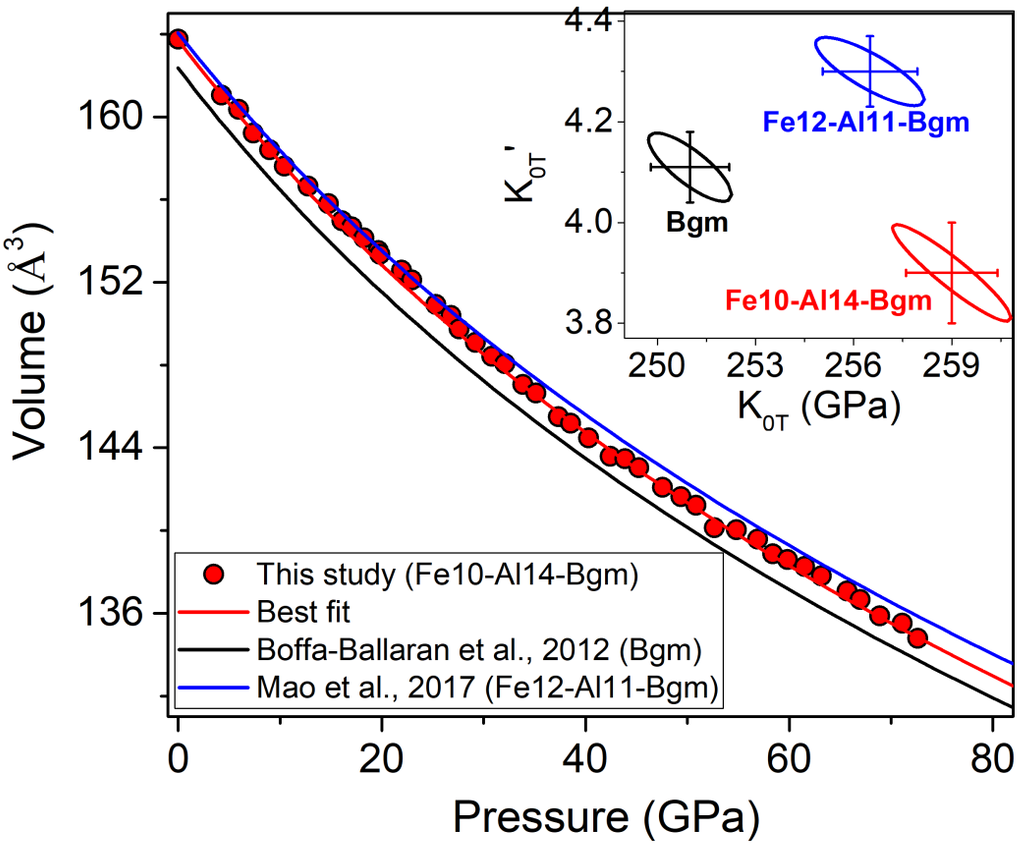

Figure S1. Unit-cell volumes of single-crystal Fe10-Al14-Bgm at high pressure and 300 K. Solid red circles are collected data of Fe10-Al14-Bgm in this study and the red line is the best fit using third-order Birch-Murnaghan EoS. Black and blue lines are literature results on $MgSiO_3$ bridgmanite end member (Boffa Ballaran et al., 2012) and (Al,Fe)-bearing bridgmanite with $Mg_{0.89}Fe^{2+}_{0.024}Fe^{3+}_{0.096}Al_{0.11}Si_{0.89}O_3$ composition (Fe12-Al11-Bgm) (Mao et al., 2017), respectively. The insert shows derived error ellipses of K_{0T} and K'_{0T} at the ±1σ level.

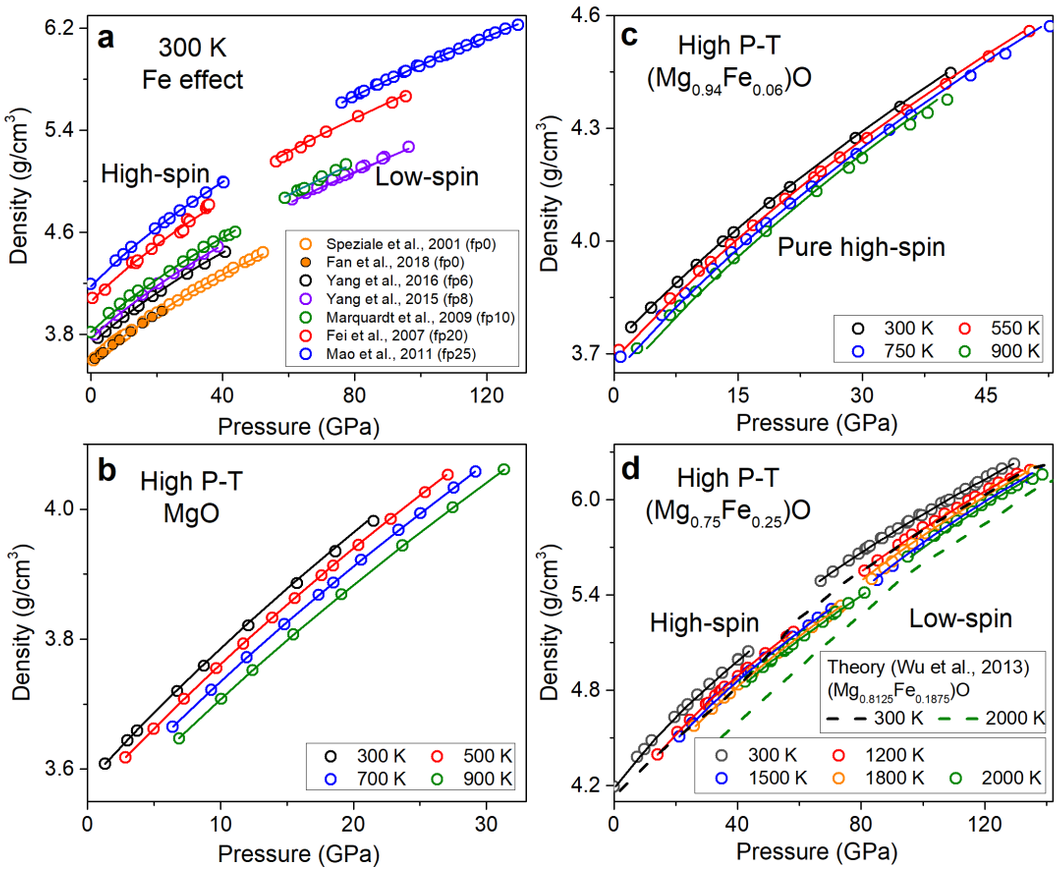

Figure S2. Modeling on thermoelastic properties of ferropericlase at high P-T. **a** is density of ferropericlase with different Fe contents at high pressure and 300 K, while **b-d** are high P-T data from the literature. In **a**, symbols are experimental data (Fei et al., 2007; Mao et al., 2011; Marquardt et al., 2009; Speziale et al., 2001; Yang et al., 2016; Yang et al., 2015), and solid lines with corresponding colors are the best fits using Birch-Murnaghan EoS. A linear Fe effect on the density of ferropericlase is assumed. Detailed references are shown in the legend, in which numbers in parentheses right after "fp" indicate its Fe content in molar per cent. In **b-d**, symbols are high P-T elastic data of MgO (Fan et al., 2019), $(Mg_{0.94}Fe_{0.06})O$ (Yang et al., 2016), and $(Mg_{0.75}Fe_{0.25})O$ (Mao et al., 2011), and solid lines are the best fits using the self-consistent thermoelastic model. Theoretical calculations on $(Mg_{0.8125}Fe_{0.1875})O$ ferropericlase (Wu et al., 2013) are plotted as dashed black (300 K) and olive (2000 K) in **d** for comparisons. Uncertainties are smaller than symbols when not shown.

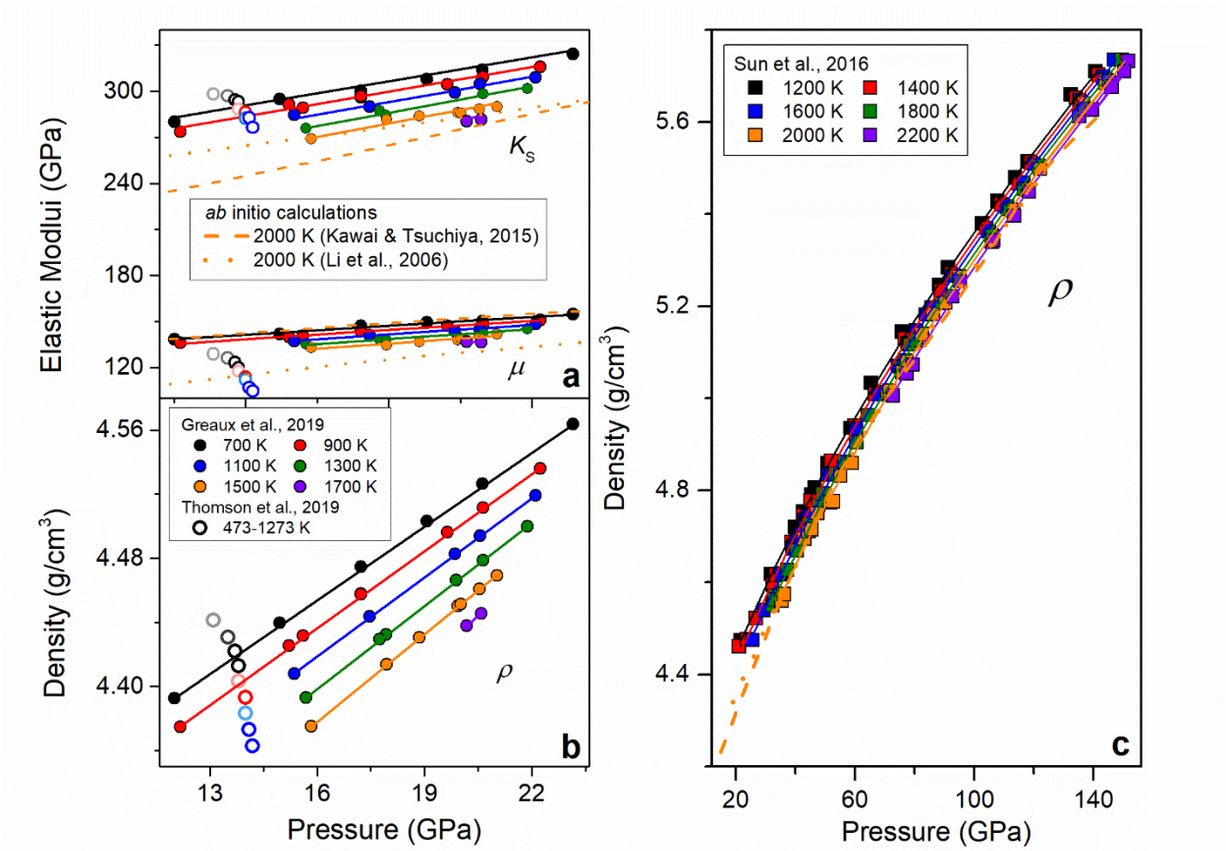

Figure S3. Modeling on thermoelastic parameters of $CaSiO_3$ davemaoite at high P-T. **a** and **b-c** show high P-T elastic moduli (K_S and μ) and density of davemaoite, respectively. In **a** and **b**, solid symbols are data from Gréaux et al. (2019), and solid lines are the best fits. Open circles are data from Thomson et al. (2019), which show much lower shear moduli than those from Gréaux et al. (2019) and are not included in our fitting. **c** is thermal EoS of $CaSiO_3$ davemaoite (Sun et al., 2016) up to 150 GPa and 2200 K, which is consistent with those by Gréaux et al. (2019) and is included in our constraints. Dashed (Kawai and Tsuchiya, 2015) and dotted (Li et al., 2006) lines are from theoretical calculations at 2000 K. Uncertainties are smaller than symbols when not shown.

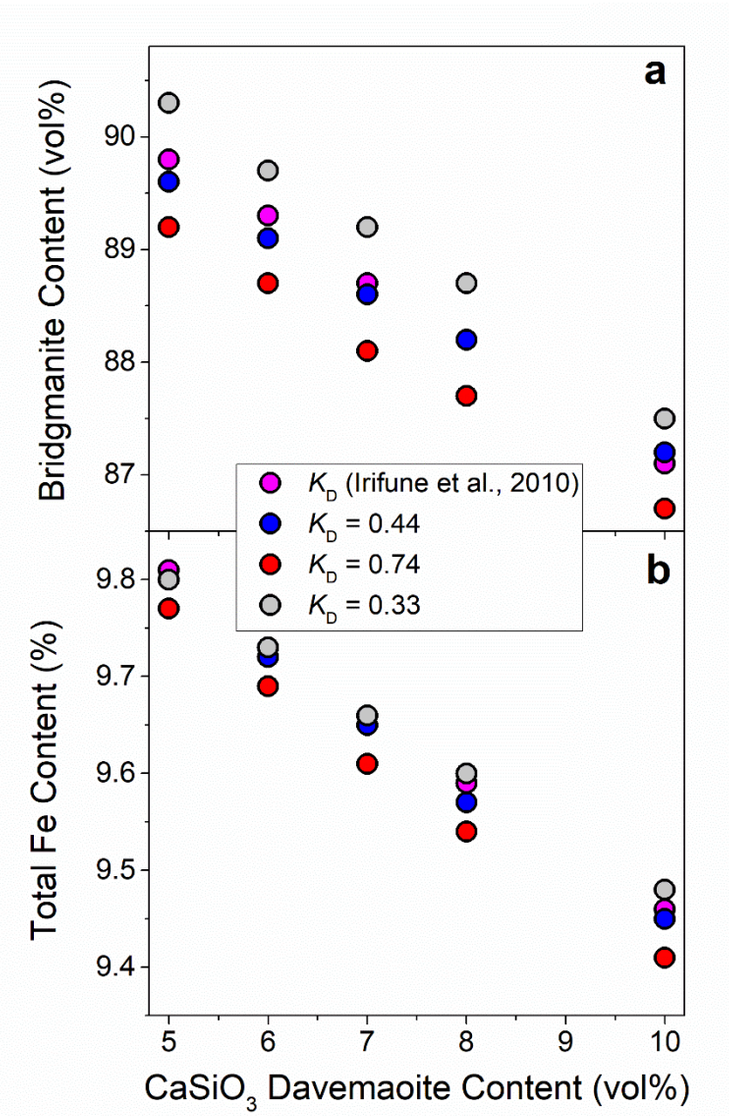

Figure S4. Trade-offs between volume and compositional parameters on deriving the lower-mantle composition. **a,** Volume percentages of bridgmanite versus $CaSiO_3$ davemaoite. **b,** Total Fe content versus the volume percentage of $CaSiO_3$ davemaoite. Pink circles are our best-fit model with K_D varying with depth (Irifune et al., 2010). Blue, red, and gray circles are results with fixed K_D as 0.44, 0.74, and 0.33, respectively. These K_D values are chosen to cover its range in literature reports (Irifune et al., 2010).

Table S1. Velocity data as a function of azimuthal angles for each platelet at all experimental high pressures. Numbers in parentheses show the ±σ uncertainties on the last digits.

	Platelet 1 (-0.50, 0.05, -0.86)			Platelet 1 (0.65, -0.59, 0.48)		
Chi angles (°)	V_P (km/s)	V_{S1} (km/s)	V_{S2} (km/s)	V_P (km/s)	V_{S1} (km/s)	V_{S2} (km/s)
			25.0 (3) GPa			
0	-	6.719(6)	6.982(6)	-	6.740(5)	-
10	-	6.547(5)	7.005(6)	-	6.594(5)	-
20	-	6.444(5)	7.066(7)	-	6.558(5)	-
30	-	6.405(5)	7.091(7)	11.66(8)	6.593(6)	-
40	-	6.420(6)	7.083(7)	11.62(8)	6.650(6)	-
50	-	6.506(6)	7.074(7)	-	-	6.820(7)
60	-	6.597(7)	7.042(8)	-	-	6.880(7)
70	-	6.774(7)	-	-	-	6.920(5)
80	-	6.749(8)	-	-	-	6.885(5)
90	-	6.751(7)	-	-	-	6.900(8)
100	11.92(6)	6.647(7)	-	-	6.580(5)	-
110	11.88(5)	6.632(7)	-	-	6.585(5)	-
120	11.84(5)	6.661(6)	-	-	6.591(5)	-
130	11.98(4)	6.693(6)	-	-	6.634(6)	-
140	12.03(4)	6.685(5)	-	-	6.749(7)	-
150	11.92(7)	6.760(5)	-	-	-	6.886(8)
160	-	6.785(5)	-	-	-	6.937(6)
170	-	6.792(6)	-	-	-	6.890(6)
180	11.54(4)	6.730(6)	-	-	6.745(7)	-
190	-	6.535(8)	7.009(6)	-	6.624(7)	-
200	11.28(7)	6.437(8)	7.068(5)	-	6.582(8)	-
			35.0 (5) GPa			
0	11.96(6)	6.774(6)	7.054(7)	-	6.813(6)	-
10	11.83(6)	6.641(6)	7.119(6)	-	6.751(6)	-
20	11.61(6)	6.623(6)	7.235(6)	-	6.688(5)	-
30	11.39(6)	6.585(6)	7.262(6)	11.89(6)	6.754(5)	-
40	11.44(5)	6.606(6)	7.259(6)	11.76(7)	6.797(5)	-
50	11.61(5)	6.623(6)	7.197(5)	-	-	6.877(7)
60	11.75(5)	6.674(7)	7.205(5)	-	-	6.986(6)
70	-	6.730(7)	7.003(7)	-	-	7.000(5)
80	-	6.868(7)	-	-	-	7.020(5)
90	12.16(4)	6.853(7)	-	-	6.620(7)	-
100	12.24(4)	6.862(7)	-	-	6.690(5)	7.050(6)
110	12.15(5)	6.870(6)	-	-	6.712(5)	-
120	-	6.866(6)	-	-	6.760(5)	-
130	12.10(5)	6.908(5)	-	-	6.811(6)	-
140	12.15(7)	6.900(5)	-	-	6.870(6)	-
150	-	6.895(5)	-	-	6.830(6)	6.990(6)
160	12.10(6)	6.911(6)	-	-	-	7.070(6)
170	-	6.903(6)	-	-	6.810(6)	7.050(7)
180	11.90(6)	6.774(6)	7.097(5)	-	6.830(6)	-
190	-	6.693(7)	7.140(5)	-	6.770(7)	-
200	11.58(8)	6.607(7)	7.250(5)	-	6.710(7)	-
			45.0 (5) GPa			

0	12.20(6)	6.984(7)	7.150(6)	-	6.970(8)	-
10	12.04(6)	6.921(8)	7.237(6)	-	6.941(8)	-
20	11.90(6)	6.873(8)	7.328(6)	-	6.952(7)	-
30	11.73(7)	6.848(8)	7.367(6)	-	6.971(7)	-
40	11.82(7)	6.812(8)	7.457(7)	-	6.996(7)	-
50	-	6.788(7)	7.363(7)	-	6.990(7)	-
60	12.04(7)	6.891(7)	7.373(8)	-	6.920(7)	7.190(7)
70	-	6.947(7)	7.249(8)	-	6.850(6)	7.230(8)
80	-	7.013(7)	-	-	6.870(6)	7.270(8)
90	-	7.036(7)	-	-	6.880(6)	7.220(7)
100	-	7.088(6)	-	-	6.890(6)	6.930(7)
110	12.37(6)	7.105(6)	-	-	6.936(7)	-
120	12.43(6)	7.134(6)	-	-	6.887(7)	-
130	12.37(6)	7.142(6)	-	-	7.020(7)	-
140	12.37(7)	7.144(6)	-	-	7.090(7)	-
150	-	7.145(6)	-	-	7.030(7)	7.220(8)
160	-	7.135(6)	-	-	6.992(8)	-
170	12.20(7)	7.090(7)	-	-	7.026(8)	-
180	12.10(7)	6.869(7)	7.249(7)	-	7.026(8)	-
190	-	6.855(6)	7.340(8)	-	6.961(6)	-
200	11.90(7)	6.833(6)	7.370(8)	-	6.944(8)	-
			54.4 (6) GPa			
0	12.38(7)	7.028(8)	7.311(7)	-	7.011(7)	-
10	12.21(7)	6.981(8)	7.380(7)	-	7.051(6)	-
20	12.10(8)	6.942(7)	7.456(7)	-	7.059(6)	-
30	11.92(8)	6.908(7)	7.520(8)	-	7.081(6)	-
40	-	6.895(7)	7.501(8)	-	7.090(6)	-
50	12.02(7)	6.924(7)	7.509(8)	-	7.086(8)	-
60	-	6.862(8)	7.393(6)	-	6.950(8)	7.140(7)
70	-	6.940(9)	7.341(6)	-	6.920(8)	7.230(7)
80	12.36(7)	7.000(9)	7.463(6)	-	6.970(8)	7.310(9)
90	12.46(8)	7.079(8)	-	-	6.930(8)	7.350(9)
100	-	7.102(8)	-	-	6.920(8)	-
110	12.62(7)	7.197(8)	-	-	7.059(8)	-
120	12.66(8)	7.274(8)	-	-	6.920(8)	-
130	12.62(8)	7.235(8)	-	-	7.081(8)	-
140	-	7.237(8)	-	-	7.090(7)	-
150	12.52(9)	7.219(7)	-	-	7.039(7)	-
160	-	7.147(7)	-	-	7.050(7)	-
170	-	7.026(6)	-	-	7.020(7)	-
180	12.36(7)	6.944(6)	7.381(7)	-	7.048(7)	-
190	12.21(8)	6.937(6)	7.479(6)	-	7.093(7)	-
200	12.10(8)	6.943(7)	7.543(8)	-	7.050(6)	-
			65.8 (8) GPa			
0	12.50(8)	7.039(7)	7.589(9)	-	7.076(7)	-
10	12.33(8)	7.086(7)	7.590(9)	-	7.030(7)	7.420(9)
20	12.20(8)	7.125(8)	7.683(9)	-	-	7.236(9)
30	-	7.122(8)	7.646(8)	-	7.070(7)	7.269(9)
40	12.10(8)	7.112(8)	7.709(8)	-	-	7.210(7)
50	-	7.104(8)	7.633(7)	-	7.122(8)	-

60	12.30(7)	7.042(8)	7.542(7)	-	7.086(8)	-
70	12.50(7)	6.997(8)	7.525(7)	-	7.135(8)	-
80	12.64(7)	7.036(9)	7.514(8)	-	7.147(8)	-
90	-	7.069(9)	-	-	7.189(8)	-
100	12.80(9)	7.212(9)	-	-	7.260(8)	-
110	-	7.316(7)	-	-	7.180(9)	7.430(8)
120	12.80(9)	7.394(8)	-	-	7.120(9)	-
130	12.80(9)	7.410(7)	-	-	7.160(7)	7.510(8)
140	-	7.359(9)	-	-	7.193(7)	-
150	12.70(9)	7.298(9)	-	-	7.136(7)	-
160	-	7.137(8)	-	-	7.140(7)	-
170	-	7.105(8)	7.50(8)	-	7.075(8)	-
180	12.53(7)	7.054(8)	7.57(8)	-	7.113(8)	-
190	12.34(7)	7.048(7)	7.57(9)	-	7.050(8)	-
200	-	7.103(7)	7.55(9)	-	7.256(8)	-
			70.4 (7) GPa			
0	12.53(9)	7.078(9)	7.603(8)	-	7.160(9)	-
10	12.40(9)	7.106(8)	7.647(9)	-	7.090(9)	-
20	-	7.175(8)	7.730(9)	-	-	7.333(9)
30	12.14(9)	7.161(8)	7.690(9)	-	-	7.280(9)
40	-	7.171(8)	7.680(9)	-	-	7.279(10)
50	12.30(8)	7.137(8)	7.671(8)	-	7.185(9)	-
60	12.36(8)	7.097(9)	7.639(8)	-	7.140(9)	-
70	-	7.063(9)	7.612(8)	-	7.121(9)	-
80	-	7.052(9)	7.541(8)	-	7.145(9)	-
90	12.80(8)	7.097(9)	7.497(9)	-	7.227(9)	-
100	-	7.293(9)	-	-	7.190(8)	7.540(10)
110	12.90(8)	7.394(9)	-	-	7.190(8)	7.510(9)
120	-	7.466(9)	-	-	7.180(8)	-
130	12.90(9)	7.490(9)	-	-	7.283(8)	7.512(8)
140	12.86(9)	7.416(8)	-	-	7.243(8)	-
150	-	7.214(8)	7.439(9)	-	7.171(8)	-
160	12.75(9)	7.144(9)	7.588(9)	-	7.160(9)	-
170	-	7.119(9)	-	-	7.115(9)	-
180	12.60(7)	7.084(10)	7.639(9)	-	7.188(9)	-
190	12.45(9)	7.134(8)	7.661(10)	-	-	7.380(9)
200	-	7.169(7)	7.692(9)	-	-	7.290(9)
			76.0 (9) GPa			
0	-	7.096(8)	7.654(10)	-	7.110(8)	7.530(10)
10	12.44(9)	7.155(9)	7.700(10)	-	-	7.410(10)
20	12.33(9)	7.252(9)	7.766(10)	-	-	7.390(10)
30	12.20(9)	7.220(10)	7.733(10)	-	-	7.320(10)
40	12.30(10)	7.239(10)	7.743(10)	-	-	7.220(9)
50	12.36(11)	7.224(10)	7.757(9)	-	7.238(9)	-
60	-	7.149(10)	7.689(9)	-	7.167(9)	-
70	-	7.105(9)	7.621(9)	-	7.163(9)	-
80	12.75(9)	7.073(9)	7.585(9)	-	7.216(9)	-
90	-	7.107(9)	7.541(9)	-	7.278(9)	-
100	12.92(9)	7.345(9)	-	-	7.300(10)	7.550(9)
110	-	7.469(9)	-	-	-	7.553(9)

120	12.92(9)	7.543(9)	-	-	-	7.544(9)
130	-	7.553(9)	-	-	7.381(10)	7.510(9)
140	12.90(8)	7.487(9)	-	-	7.318(9)	-
150	-	7.377(9)	-	-	7.239(9)	-
160	12.80(8)	7.185(9)	7.655(10)	-	7.135(9)	-
170	-	7.170(10)	7.683(10)	-	7.137(9)	-
180	-	7.135(10)	7.733(10)	-	7.160(9)	-
190	12.47(9)	7.174(10)	7.757(11)	-	-	7.410(9)
200	12.33(9)	7.206(10)	7.747(10)	-	-	7.390(9)
			82.0 (14) GPa			
0	-	7.113(10)	7.705(11)	-	7.302(9)	-
10	12.54(10)	7.205(10)	7.752(11)	-	-	7.531(11)
20	12.38(10)	7.329(10)	7.803(11)	-	-	7.570(11)
30	12.27(10)	7.325(12)	7.776(11)	-	-	7.680(11)
40	12.38(10)	7.306(12)	7.806(12)	-	7.196(9)	7.614(12)
50	12.49(11)	7.311(11)	7.843(12)	-	7.103(10)	7.560(12)
60	-	7.202(11)	7.740(12)	-	7.080(10)	-
70	12.71(11)	7.147(11)	7.630(12)	-	7.050(10)	-
80	-	7.094(12)	7.628(10)	-	-	7.275(11)
90	-	7.111(12)	7.710(10)	-	-	7.300(13)
100	12.94(12)	7.478(12)	-	-	7.433(11)	7.550(13)
110	-	7.617(11)	-	-	7.605(11)	-
120	13.00(12)	7.701(11)	-	-	7.400(11)	-
130	13.00(12)	7.705(12)	-	-	7.435(10)	7.510(11)
140	-	7.646(9)	-	-	7.391(9)	-
150	12.94(9)	7.313(9)	-	-	7.322(9)	-
160	-	7.236(9)	7.730(10)	-	7.265(9)	-
170	12.82(11)	7.171(9)	7.776(10)	-	7.298(11)	-
180	-	7.186(9)	7.716(10)	-	7.246(10)	-
190	-	7.253(10)	7.800(12)	-	-	7.601(10)
200	-	7.330(9)	7.840(11)	-	-	7.610(10)

Table S2. Unit-cell parameters of single-crystal Fe10-Al14-Bgm at high pressure

Au		Fe10-Al14-Bgm			
Pressure (GPa)	*a* (Å)	*a* (Å)	*b* (Å)	*c* (Å)	*V* (Å^3)
ambient		4.7875(2)	4.9423(2)	6.9205(2)	163.75(1)
4.3(1)	4.0463(3)	4.7601(2)	4.9122(2)	6.8873(2)	161.04(1)
5.9(1)	4.0348(3)	4.7526(2)	4.9056(2)	6.8776(2)	160.35(1)
7.4(1)	4.0253(3)	4.7375(2)	4.9029(2)	6.8544(2)	159.21(1)
9.0(1)	4.0151(3)	4.7282(2)	4.8971(2)	6.8410(2)	158.40(2)
10.4(1)	4.0064(3)	4.7244(2)	4.8868(2)	6.8269(3)	157.62(2)
12.8(1)	3.9930(3)	4.7131(2)	4.8805(2)	6.8099(3)	156.64(2)
14.8(1)	3.9820(3)	4.7023(3)	4.8745(2)	6.7969(3)	155.79(2)
16.1(1)	3.9750(3)	4.6967(3)	4.8638(2)	6.7845(3)	154.98(2)
17.1(1)	3.9701(3)	4.6952(3)	4.8599(2)	6.7782(3)	154.67(2)
18.3(1)	3.9640(3)	4.6897(3)	4.8538(2)	6.7720(3)	154.15(2)
19.6(1)	3.9573(3)	4.6821(3)	4.8483(2)	6.7640(3)	153.54(3)
19.8(1)	3.9564(3)	4.6812(3)	4.8455(2)	6.7605(3)	153.35(3)
21.9(1)	3.9464(3)	4.6744(3)	4.8403(3)	6.7436(3)	152.58(3)
22.9(1)	3.9418(3)	4.6678(3)	4.8357(3)	6.7390(3)	152.11(3)
25.3(1)	3.9313(3)	4.6623(3)	4.8143(3)	6.7239(3)	150.92(3)
26.8(1)	3.9249(3)	4.6562(3)	4.8113(3)	6.7136(4)	150.40(4)
27.6(2)	3.9217(4)	4.6485(3)	4.8034(3)	6.7061(4)	149.74(4)
29.2(2)	3.9150(4)	4.6406(3)	4.7962(3)	6.6985(4)	149.09(4)
30.8(2)	3.9086(4)	4.6316(3)	4.7906(3)	6.6894(4)	148.42(4)
32.1(2)	3.9036(5)	4.6364(3)	4.7873(3)	6.6709(4)	148.06(4)
33.8(2)	3.8969(6)	4.6143(3)	4.7812(3)	6.6660(4)	147.06(5)
35.1(2)	3.8920(6)	4.6204(4)	4.7689(3)	6.6555(4)	146.65(5)
37.3(2)	3.8840(6)	4.5977(4)	4.7574(3)	6.6488(5)	145.50(5)
38.6(3)	3.8797(7)	4.5989(4)	4.7566(3)	6.6374(5)	145.19(5)
40.3(3)	3.8736(8)	4.5913(4)	4.7502(3)	6.6246(5)	144.48(5)
42.4(3)	3.8664(9)	4.5813(4)	4.7412(3)	6.6110(5)	143.59(5)
43.9(3)	3.8617(9)	4.5848(4)	4.7477(3)	6.5905(5)	143.46(6)
45.2(4)	3.857310)	4.5800(4)	4.7424(4)	6.5850(5)	143.03(6)
47.6(4)	3.8498(10)	4.5676(4)	4.7356(4)	6.5691(5)	142.09(6)
49.4(4)	3.8443(10)	4.5645(4)	4.7286(4)	6.5622(5)	141.64(6)
50.8(4)	3.8398(11)	4.5562(5)	4.7266(4)	6.5574(5)	141.22(6)
52.7(4)	3.8344(10)	4.5494(5)	4.7102(4)	6.5396(6)	140.13(6)
54.8(4)	3.8281(11)	4.5464(5)	4.7109(4)	6.5382(6)	140.03(6)
56.9(5)	3.8222(11)	4.5358(5)	4.7042(4)	6.5410(6)	139.57(6)
58.4(5)	3.8181(11)	4.5236(5)	4.7000(4)	6.5314(6)	138.86(7)
59.9(5)	3.8141(11)	4.5225(6)	4.6956(4)	6.5266(6)	138.60(7)
61.5(5)	3.8097(11)	4.5172(6)	4.6938(5)	6.5205(6)	138.26(7)
63.1(5)	3.8053(11)	4.5080(6)	4.6910(5)	6.5163(6)	137.80(7)
65.7(4)	3.7987(10)	4.4973(6)	4.6823(5)	6.5091(6)	137.07(7)
67.0(5)	3.7954(10)	4.4877(6)	4.6814(5)	6.5046(6)	136.66(7)
68.9(5)	3.7907(10)	4.4701(6)	4.6766(5)	6.4994(7)	135.87(7)
71.1(5)	3.7853(11)	4.4719(6)	4.6700(5)	6.4887(7)	135.51(7)
72.6(5)	3.7816(11)	4.4567(6)	4.6661(5)	6.4810(7)	134.78(7)

Table S3. Thermoelastic parameters of lower-mantle major minerals for high P-T modeling

	V_0 (Å^3)	K_0 (GPa)	K'_0	μ_0 (GPa)	μ'_0	θ_0	γ_0	q_0	η_{S0}
[a](Al,Fe)-bearing Bridgmanite	-	-	-	-	-	900	1.57	1.1	2.4
[a]Ferropericlase (HS)	-	-	-	-	-	760	1.4	1.2	2.6
[a]Ferropericlase (LS)	-	-	-	-	-	760	1.4	0.3	2.6
[b]$CaSiO_3$ davemaoite	45.4	248	4	126	1.6	1000	1.42	2.65	1.54

[a]See details in main text and supplementary text S2 for Fe and/or Al effects on V_0, K_0, K'_0, μ_0, and μ'_0 of (Al,Fe)-bearing bridgmanite and ferropericlase. Values of θ_0, q_0, γ_0, and η_{S0} for (Al,Fe)-bearing bridgmanite and ferropericlase are constrained by benchmarking from literature experimental data together with *ab initio* calculations (Fiquet et al., 2000; Mao et al., 2011; Shim and Duffy, 2000; Stixrude and Lithgow-Bertelloni, 2005; Tange et al., 2012; Wentzcovitch et al., 2004; Wolf et al., 2015).

[b]Thermoelastic parameters for $CaSiO_3$ davemaoite are derived by refitting literature data (Gréaux et al., 2019; Sun et al., 2016) with the model.

References

Birch, F., 1978. Finite Strain Isotherm and Velocities for Single-Crystal and Polycrystalline Nacl at High-Pressures and 300-Degree-K. Journal of Geophysical Research 83, 1257-1268.

Boffa Ballaran, T., Kurnosov, A., Glazyrin, K., Frost, D.J., Merlini, M., Hanfland, M., Caracas, R., 2012. Effect of chemistry on the compressibility of silicate perovskite in the lower mantle. Earth and Planetary Science Letters 333, 181-190.

Fan, D., Fu, S., Yang, J., Tkachev, S.N., Prakapenka, V.B., Lin, J.-F., 2019. Elasticity of single-crystal periclase at high pressure and temperature: The effect of iron on the elasticity and seismic parameters of ferropericlase in the lower mantle. American Mineralogist: Journal of Earth and Planetary Materials 104, 262-275.

Fei, Y.W., Zhang, L., Corgne, A., Watson, H., Ricolleau, A., Meng, Y., Prakapenka, V., 2007. Spin transition and equations of state of (Mg,Fe)O solid solutions. Geophysical Research Letters 34.

Fiquet, G., Dewaele, A., Andrault, D., Kunz, M., Le Bihan, T., 2000. Thermoelastic properties and crystal structure of $MgSiO_3$ perovskite at lower mantle pressure and temperature conditions. Geophysical Research Letters 27, 21-24.

Gréaux, S., Irifune, T., Higo, Y., Tange, Y., Arimoto, T., Liu, Z., Yamada, A., 2019. Sound velocity of $CaSiO_3$ perovskite suggests the presence of basaltic crust in the Earth's lower mantle. Nature 565, 218.

Irifune, T., Shinmei, T., McCammon, C.A., Miyajima, N., Rubie, D.C., Frost, D.J., 2010. Iron partitioning and density changes of pyrolite in Earth's lower mantle. Science 327, 193-195.

Kawai, K., Tsuchiya, T., 2015. Small shear modulus of cubic CaSiO3 perovskite. Geophysical Research Letters 42, 2718-2726.

Li, L., Weidner, D.J., Brodholt, J., Alfe, D., Price, G.D., Caracas, R., Wentzcovitch, R., 2006. Elasticity of $CaSiO_3$ perovskite at high pressure and high temperature. Physics of the Earth and Planetary Interiors 155, 249-259.

Mao, Z., Lin, J.F., Liu, J., Prakapenka, V.B., 2011. Thermal equation of state of lower-mantle ferropericlase across the spin crossover. Geophysical Research Letters 38.

Mao, Z., Wang, F., Lin, J.-F., Fu, S., Yang, J., Wu, X., Okuchi, T., Tomioka, N., Prakapenka, V.B., Xiao, Y., 2017. Equation of state and hyperfine parameters of high-spin bridgmanite in the Earth's lower mantle by synchrotron X-ray diffraction and Mössbauer spectroscopy. American Mineralogist 102, 357-368.

Marquardt, H., Speziale, S., Reichmann, H.J., Frost, D.J., Schilling, F.R., 2009. Single-crystal elasticity of $(Mg_{0.9}Fe_{0.1})O$ to 81 GPa. Earth and Planetary Science Letters 287, 345-352.

Shim, S.-H., Duffy, T.S., 2000. Constraints on the PVT equation of state of MgSiO3 perovskite. American Mineralogist 85, 354-363.

Speziale, S., Lee, V.E., Clark, S.M., Lin, J.F., Pasternak, M.P., Jeanloz, R., 2007. Effects of Fe spin transition on the elasticity of (Mg,Fe)O magnesiowustites and implications for the seismological properties of the Earth's lower mantle. Journal of Geophysical Research-Solid Earth 112.

Speziale, S., Zha, C.S., Duffy, T.S., Hemley, R.J., Mao, H.k., 2001. Quasi-hydrostatic compression of magnesium oxide to 52 GPa: Implications for the pressure-volume-temperature equation of state. Journal of Geophysical Research: Solid Earth 106, 515-528.

Stixrude, L., Lithgow-Bertelloni, C., 2005. Thermodynamics of mantle minerals—I. Physical properties. Geophysical Journal International 162, 610-632.

Sun, N., Mao, Z., Yan, S., Wu, X., Prakapenka, V.B., Lin, J.F., 2016. Confirming a pyrolitic lower mantle using self-consistent pressure scales and new constraints on $CaSiO_3$ perovskite. Journal of Geophysical Research: Solid Earth 121, 4876-4894.

Tange, Y., Kuwayama, Y., Irifune, T., Funakoshi, K.i., Ohishi, Y., 2012. P-V-T equation of state of $MgSiO_3$ perovskite based on the MgO pressure scale: A comprehensive reference for mineralogy of the lower mantle. Journal of Geophysical Research: Solid Earth 117.

Thomson, A.R., Crichton, W.A., Brodholt, J.P., Wood, I.G., Siersch, N.C., Muir, J.M.R., Dobson, D.P., Hunt, S.A., 2019. Seismic velocities of CaSiO3 perovskite can explain LLSVPs in Earth's lower mantle. Nature.

Wentzcovitch, R., Karki, B., Cococcioni, M., De Gironcoli, S., 2004. Thermoelastic Properties of $MgSiO_3$-Perovskite: Insights on the Nature of the Earth's Lower Mantle. Physical review letters 92, 018501.

Wolf, A.S., Jackson, J.M., Dera, P., Prakapenka, V.B., 2015. The thermal equation of state of (Mg,Fe)SiO_3 bridgmanite (perovskite) and implications for lower mantle structures. Journal of Geophysical Research-Solid Earth 120, 7460-7489.

Wu, Z.Q., Justo, J.F., Wentzcovitch, R.M., 2013. Elastic Anomalies in a Spin-Crossover System: Ferropericlase at Lower Mantle Conditions. Physical Review Letters 110.

Yang, J., Lin, J.F., Jacobsen, S.D., Seymour, N.M., Tkachev, S.N., Prakapenka, V.B., 2016. Elasticity of ferropericlase and seismic heterogeneity in the Earth's lower mantle. Journal of Geophysical Research: Solid Earth.

Yang, J., Tong, X.Y., Lin, J.F., Okuchi, T., Tomioka, N., 2015. Elasticity of Ferropericlase across the Spin Crossover in the Earth's Lower Mantle. Scientific Reports 5.